Journal of Computational Physics **151,** 921–946 (1999)
Article ID jcph.1999.6227, available online at http://www.idealibrary.com on IDEAL®

An Analysis of the Discontinuous Galerkin Method for Wave Propagation Problems

Fang Q. Hu,* M. Y. Hussaini,† and Patrick Rasetarinera†

*Department of Mathematics and Statistics, Old Dominion University, Norfolk, Virginia 23529; and †Program in Computational Science and Engineering, Florida State University, Tallahassee, Florida 32306-4120
E-mail: fang@math.odu.edu, myh@cse.fsu.edu, rasetari@cse.fsu.edu

Received September 21, 1998; revised February 2, 1999

The dispersion and dissipation properties of the discontinuous Galerkin method are investigated with a view to simulating wave propagation phenomena. These properties are analysed in the semi-discrete context of the one-dimensional scalar advection equation and the two-dimensional wave equation, discretized on triangular and quadrilateral elements. They are verified by the results from full numerical solutions of the simple scalar advection equation and the Euler equations.

Key Words: discontinuous Galerkin method; wave propagation; dissipation, dispersion and anisotropy errors.

1. INTRODUCTION

The discontinuous Galerkin method appears to have been first proposed by Reed and Hill [28] for the solution of the linear neutron transport equation. Lesaint and Raviart [21] were the first to put this method on a firm mathematical basis. Among the later rigorous analyses of the method are those of Johnson and Pitkäranta [19], Richter [29], Peterson [27], and Bey and Oden [4]. All these studies are confined to linear equations. The first analysis of this method as applied to a non-linear scalar hyperbolic equation is due to Chavent and Cockburn [7]. It was first-order accurate in time and second-order accurate in space. In [9], Cockburn and Shu retained the finite element formulation of [7] but used a second-order Runge–Kutta type discretization in time. Subsequently, they generalized it to a class of discontinuous Galerkin methods of arbitrary order of formal accuracy and proved their convergence and total-variation boundedness in the mean [10]. Then Cockburn *et al.* [11] extended their analysis to a one-dimensional system of conservation laws, and Cockburn *et al.* [12] further extended it to the multidimensional scalar case, and more recently Cockburn and Shu treated the multidimesional systems case [13]. These schemes essentially

0021-9991/99 $30.00

employ a discontinuous element formulation and an explicit Runge–Kutta time discretization and have proven to be inherently compact and robust; a quadrature free formulation of these schemes is described by Atkins and Shu [2]. They apply it to the inviscid Burgers equation and to some one-dimensional and two-dimensional linear advection problems, including the linearized Euler equations for acoustics. They show that this formulation requires comparatively less storage and computational time than their conventional counterpart. In [3] Bassi and Rebay extended the discontinuous Galerkin method to the compressible Navier–Stokes equations. In their formulation, the solution and its gradient are approximated in the same function space, thereby preserving compactness. They illustrate the performance of the method for supersonic flow past an airfoil (at rather low Reynolds number) using constant, linear, quadratic, and cubic elements. Cockburn and Shu [14] have also extended their approach to deal with the time-dependent scalar advection–diffusion equation by rewriting the equation as a degenerate first-order system and have suggested how the approach could be applied to the Navier–Stokes equations. The amenability of the method with discontinuous spatial elements for parallel computation has been established by Biswas *et al.* [5]. Thus, while the inherent flexibility of such schemes to handle complex geometry and their compactness are obvious, their robustness and ease in accommodating boundary conditions and parallel implementation have been demonstrated by the above studies.

It is well recognized that highly accurate methods are needed for long-time simulations of wave propagation phenomena in acoustics and electromagnetics, which are essentially non-dispersive and non-dissipative [16, 17]. Many current numerical schemes employed to study such problems are of the finite difference type [20, 22, 31, 33]. Finite element methods have also been advocated by numerous authors (see, for example, [6, 25, 26]). The properties of such methods for the Helmholtz problem have been widely studied [1, 34, 36]. For hyperbolic problems, Shakib and Hughes [30] provide a Fourier analysis of the space-time Galerkin/least-squares method. The analysis of the Taylor–Galerkin method in one dimension has been proposed by Khelifa and Ouellet [18] and Chaffin and Baker [8]. In these methods, the space discretization is continuous so the inversion of a global mass matrix is generaly required. The discontinuous Galerkin method provides an attractive alternative. Lowrie [23] and Lowrie *et al.* [24] considered the space–time discontinuous Galerkin which involves discontinuous elements in both time and space. In [23] a Fourier analysis of the scheme was performed which shows a "superconvergence" property; i.e., the evolution error is $O(h^{2k+1})$ if the order of the polynomial space used is k. Nevertheless the method requires excessive resources to be useful for practical applications. In this paper, we investigate the wave propagation properties of the semi-discrete form of the discontinuous Galerkin method. We study the dissipation, dispersion, and anisotropy errors introduced by the space discretization and examine these errors on Cartesian and triangular grids.

We provide a brief description of the discontinuous Galerkin method in Section 2. An analysis of wave propagation in one dimension and two dimensions is carried out in Section 3. In the two-dimensional case, the study is based on a structured rectangular and triangular grid. Section 4 contains several numerical examples for the one-dimensional advection equation and the two-dimensional non-linear Euler equations, which validate the analysis. Some numerical results from the simulation on an unstructured grid are also presented. The last section discusses the conclusions.

2. DISCONTINUOUS GALERKIN METHOD

Consider a conservation equation for a quantity $\mathbf{u}$ in a region $\mathcal{D}$

$$\frac{\partial \mathbf{u}}{\partial t} + \nabla \cdot \mathbf{F}(\mathbf{u}) = 0, \tag{2.1}$$

where $\mathbf{F}(\mathbf{u})$ is a flux vector. Let the domain be partitioned into non-overlapping sub-domains, or elements, $\mathcal{D}_i$. The discontinuous Galerkin method is a finite element method in which the approximation space V_h may be discontinuous across element interfaces. In the semi-discrete formulation, V_h contains only spatial functions

$$V_h = \{v \in L^1(\mathcal{D}) : v \,|\, \mathcal{D}_i \in \mathcal{P}(\mathcal{D}_i)\},$$

where $\mathcal{P}(\mathcal{D}_i)$ is a polynomial space defined on $\mathcal{D}_i$. The degrees of freedom of the solution are then obtained by solving a weak formulation of (2.1).

Let $\mathcal{B}_i = \{v_l^i\}_{l=0,\ldots,N-1}$ be a local basis set such that

$$\text{Span}(\mathcal{B}_i) = \mathcal{P}(\mathcal{D}_i), \qquad \text{Supp}\big(v_l^i(\mathbf{x})\big) = \mathcal{D}_i, \qquad l = 0, \ldots, N-1.$$

Then the approximate solution $\mathbf{u}_h$ satisfies

$$\int_{\mathcal{D}_i} \mathbf{v}_l^i \left(\frac{\partial \mathbf{u}_h}{\partial t} + \nabla \cdot \mathbf{F}(\mathbf{u}_h) \right) d\mathbf{x} = 0, \qquad l = 0, \ldots, N-1 \tag{2.2}$$

in each element $\mathcal{D}_i$. Using Green's formula, Eq. (2.2) is recast as

$$\int_{\mathcal{D}_i} \mathbf{v}_l^i \frac{\partial \mathbf{u}_h}{\partial t} - \nabla \mathbf{v}_l^i \cdot \mathbf{F}(\mathbf{u}_h)\, d\mathbf{x} + \int_{\partial \mathcal{D}_i} \mathbf{v}_l^i \mathbf{F}(\mathbf{u}_h) \cdot \mathbf{n}\, ds = 0, \qquad l = 0, \ldots, N-1, \tag{2.3}$$

where $\partial \mathcal{D}_i$ is the boundary of $\mathcal{D}_i$ and $\mathbf{n}$ denotes the unit outward normal vector. Since the data are discontinuous across the interface of contiguous domains, two values of $\mathbf{u}_h$ ($\mathbf{u}_h^i$ inside $\mathcal{D}_i$ and $\mathbf{u}_h^j$ outside $\mathcal{D}_i$) are available at the interface. A numerical flux $\mathbf{F}_{\text{num}}$ is then used to evaluate the interface flux in the last integral of Eq. (2.3)

$$\mathbf{F}(\mathbf{u}_h) \cdot \mathbf{n} \,|_{\,\partial \mathcal{D}_i} = \mathbf{F}_{\text{num}}\big(\mathbf{u}_h^i, \mathbf{u}_h^j, \mathbf{n}\big).$$

The above formulation can be interpreted as a standard Galerkin method in each element with a weak boundary condition. Johnson and Pitkäranta [19] have shown that the order of accuracy of the method is at least $n + 1/2$ if polynomials of degree at most n are used as basis functions. However, Lesaint and Raviart [21] and Richter [29] proved that the order of accuracy is $(n+1)$ on a Cartesian grid and on a semi-uniform triangular grid, respectively. For simplicity, we call the method to be $(n+1)$th order if the basis functions are polynomials of degree at most n.

3. WAVE PROPAGATION ANALYSIS

To study the wave propagation properties of the semi-discrete discontinuous Galerkin method described above, we consider the conservation law (2.1) with the linear flux

$$\mathbf{F}(\mathbf{u}) = (A_1\mathbf{u}, \ldots, A_d\mathbf{u}), \qquad \mathbf{u} = (u_1, \ldots, u_m), \tag{3.1}$$

where d is the number of space dimensions and $A_{i=1,\ldots,d}$ are constant $m \times m$ real matrices such that any real combination of the A_i has real eigenvalues.

As the problem is linear, the standard numerical fluxes may be written as

$$\mathbf{F}_{\text{num}}(\mathbf{u}_1, \mathbf{u}_2, \mathbf{n}) = \tilde{A}_\alpha^+ \mathbf{u}_1 + \tilde{A}_\alpha^- \mathbf{u}_2 \qquad \text{with } \tilde{A} = \sum_{k=1}^{d} A_k n_k,$$

where

$$\tilde{A}_\alpha^+ = \frac{\tilde{A} + \alpha|\tilde{A}|}{2}; \qquad \tilde{A}_\alpha^- = \frac{\tilde{A} - \alpha|\tilde{A}|}{2},$$

and α is a real positive number. The case $\alpha = 0$ corresponds to a centered flux and $\alpha = 1$ corresponds to the Roe flux (which, since the problem is linear, is the same as the Godunov flux [15] or the Steger–Warming flux [32]).

Assuming an unbounded domain $\mathcal{D}$ and writing the local approximate solution $\mathbf{u}_h$ in $\mathcal{D}_i$ as an expansion of the local basis set $\mathcal{B}_i$

$$\mathbf{u}_h|_{\mathcal{D}_i}(\mathbf{x}, t) = \sum_{l=0}^{N-1} \mathbf{C}_l^i(t) v_l^i(\mathbf{x}),$$

where $\mathbf{C}_l^i$ are the expansion coefficients or the degrees of freedom for the solution in $\mathcal{D}_i$; Eq. (2.3) then reads

$$\sum_{l=0}^{N-1} \left\{ \frac{\partial \mathbf{C}_l^i}{\partial t} \int_{\mathcal{D}_i} v_l^i v_{l'}^i \, d\mathbf{x} - \sum_{k=1}^{d} A_k \mathbf{C}_l^i \int_{\mathcal{D}_i} v_l^i \frac{\partial v_{l'}^i}{\partial x_k} \, d\mathbf{x} + \sum_{j \in Nb(\mathcal{D}_i)} \tilde{A}_\alpha^+ \mathbf{C}_l^i \int_{S_{ij}} v_l^i v_{l'}^i \, ds \right.$$
$$\left. + \tilde{A}_\alpha^- \mathbf{C}_l^j \int_{S_{ij}} v_l^j v_{l'}^i \, ds \right\} = 0, \qquad l' = 0, \ldots, N-1 \tag{3.2}$$

with

$$Nb(\mathcal{D}_i) = \{j, \ j \neq i : S_{ij} \neq \emptyset\} \qquad \text{and} \qquad S_{ij} = \partial\mathcal{D}_i \cap \partial\mathcal{D}_j.$$

To compute the dispersion relation of the scheme, we seek a solution in the usual form

$$\mathbf{u}(\mathbf{x}, t) = \hat{\mathbf{u}} \, e^{i(\mathbf{k}\cdot\mathbf{x} - \omega t)}, \tag{3.3}$$

which represents a sinusoidal wave train with a wave number $\mathbf{k}$ and a frequency ω. First an unbounded domain is generated by repeating a mesh pattern (Fig. 11). Then the expansion coefficients $\mathbf{C}_l^i$ of the solution are calculated by projecting (3.3) onto the local basis of the elements in the mesh as

$$\mathbf{C}_l^i(t) = \hat{\mathbf{u}} \, \frac{\int_{\mathcal{D}_i} v_l^i(\xi) e^{(i\mathbf{k}\xi - \omega t)} d\xi}{\int_{\mathcal{D}_i} \left(v_l^i\right)^2(\xi) d\xi}, \qquad l = 0, \ldots, N-1.$$

Since the mesh is structured, for each element there exists a translation which maps a reference element $\hat{\mathcal{D}}$ onto the element $\mathcal{D}_i$ such that

$$X = \hat{X} + \mathbf{x}_i, \qquad \mathbf{x}_i \in \mathcal{D}_i, X \in \mathcal{D}_i, \hat{X} \in \hat{\mathcal{D}}.$$

We then have

$$\mathbf{C}_l^i(t) = \hat{\mathbf{C}}_l^i e^{(i\mathbf{k}\cdot\mathbf{x}_i - \omega t)},$$

with

$$\hat{\mathbf{C}}_l^i = \hat{\mathbf{u}} \frac{\int_{\hat{\mathcal{D}}} v_l(\xi) e^{i\mathbf{k}\xi} d\xi}{\int_{\hat{\mathcal{D}}} v_l^2(\xi) d\xi}, \qquad l = 0, \ldots, N-1.$$

The algebraic system which results from (3.2) gives the numerical dispersion relation for the semi-discrete scheme.

3.1. One-Dimensional Analysis

In this Section, we analyze the dissipation and dispersion errors in the semi-discretization of the one-dimensional scalar advection equation

$$\frac{\partial u}{\partial t} + a\frac{\partial u}{\partial x} = 0, \qquad -\infty < x < \infty \tag{3.4}$$

$$u(x, 0) = e^{ikx}, \tag{3.5}$$

where the wave speed a is a positive real number. The exact dispersion relation for (3.4) corresponding to its elementary solution (3.3) is $\omega = ak$.

Let the domain be partitioned into elements, $I_n = [x_n, x_{n+1}]$, where

$$\cdots < x_{-2} < x_{-1} < x_0 < x_1 < x_2 < \cdots.$$

Using an upwind numerical flux ($\alpha = 1$), we can write Eq. (3.2) in the matrix form

$$\frac{\Delta x_n}{2}\mathbf{Q}\frac{\partial \mathbf{C}^n}{\partial t} + a\mathbf{N}_{-1}\mathbf{C}^{n-1} + a\mathbf{N}_0\mathbf{C}^n = 0, \tag{3.6}$$

where $\mathbf{C}^n = (C_0^n, C_1^n, \ldots, C_{N-1}^n)^{\mathrm{T}}$ are the expansion coefficients in the element I_n; $\Delta x_n \equiv x_{n+1} - x_n$; and the matrices $\mathbf{Q}$, $\mathbf{N}_{-1}$, and $\mathbf{N}_0$ are given in the Appendix.

If the mesh is uniform, i.e., $\Delta x_n \equiv \delta$ and $x_n = n\delta$, then we can seek solutions of the form

$$\mathbf{C}^n(t) = \hat{\mathbf{C}} e^{i(kn\delta - \omega t)} \tag{3.7}$$

which satisfy the initial condition (3.5) where $\hat{\mathbf{C}}$ is a complex vector of dimension N independent of n and t. By substituting (3.7) into (3.6), we get an algebraic system for $\hat{\mathbf{C}}$

$$\left(-\frac{i\omega\delta}{2}\mathbf{Q} + ae^{-ik\delta}\mathbf{N}_{-1} + a\mathbf{N}_0\right)\hat{\mathbf{C}} = 0. \tag{3.8}$$

It is clear that $\hat{\mathbf{C}}$ is an eigenvector corresponding to the eigenvalue ω of the matrix

$$\mathbf{M} = \frac{2}{i\delta}\mathbf{Q}^{-1}\left(ae^{-ik\delta}\mathbf{N}_{-1} + a\mathbf{N}_0\right).$$

For a given value of the wave number k, the matrix $\mathbf{M}$ has N eigenvalues $\{\omega_l\}_{l=0,\ldots,N-1}$ and

N eigenvectors $\{\hat{\mathbf{C}}_l\}_{l=0,\ldots,N-1}$. Therefore, we can write the solution (3.7) as

$$\mathbf{C}^n(t) = \sum_{l=0}^{N-1} \lambda_l \hat{\mathbf{C}}_l e^{i(kn\delta - \omega_l t)}, \tag{3.9}$$

where λ_l are the scaling coefficients such that (3.9) satisfies the initial condition (3.5)

$$\hat{\mathbf{C}}_{ex} = \sum_{l=0}^{N-1} \lambda_l \hat{\mathbf{C}}_l$$

with $\hat{\mathbf{C}}_{ex} = (\hat{c}_{ex,0}, \hat{c}_{ex,1}, \ldots, \hat{c}_{ex,N-1})^{\mathrm{T}}$ and

$$\hat{c}_{ex,l} = \frac{\int_0^\delta v_l(\xi) e^{ik\xi} d\xi}{\int_0^\delta v_l^2(\xi) d\xi}, \qquad l = 0, \ldots, N-1.$$

The numerical solution (3.9) is a superposition of N waves traveling at different phase speeds. We define the *physical mode* as one with the frequency that approximates the exact dispersion relation for a range of wave numbers. The others are the *parasite modes* associated with the numerical scheme.

Dissipation and dispersion errors. Define the non-dimensional wave number and frequency as

$$K = k\delta \qquad \text{and} \qquad \Omega = \frac{\omega\delta}{a}. \tag{3.10}$$

The numerical dispersion relation is determined from (3.8) as

$$\det(-i\Omega\mathbf{Q} + 2e^{-iK}\mathbf{N}_{-1} + 2\mathbf{N}_0) = 0 \tag{3.11}$$

whereas the exact dispersion relation is $\Omega = K$. The values of Ω are generally complex, $\Omega = \Omega_r + i\Omega_i$, with a negative imaginary part. The negative imaginary part represents the numerical damping inherent in the discretization process.

The solution of (3.11) for a third-order discontinuous Galerkin method involves three modes. Figure 1 shows the dispersion relation Ω_r vs K for these modes. We can see that the physical mode, plotted as a solid line, agrees with the exact dispersion relation up to approximately $K = 3$. As the wave number increases beyond 3, the damping rate of the physical mode increases and the real part of Ω also starts to deviate from the exact value. The two parasite modes associated with the numerical scheme (3.6) are shown as dashed lines in Fig. 1. Note that the dissipation rate of the parasite waves is relatively large for the resolved range of wave numbers. As such, they are quickly damped for this range of wave numbers. A detailed study of these parasite waves will be given elsewhere.

In Fig. 2, the numerical dispersion relation of the physical mode is plotted for schemes of order 2 to 6. For the purpose of comparison between the schemes of different orders, the wave number K is normalized by the order of the scheme N. It is to be noted that the dispersion relation deviates from the exact one beyond $K \approx N$. Also, increasing the order of the scheme significantly reduces the dissipation error. This figure also indicates that the sixth-order scheme is optimal for the scalar advection in that it is of minimal order for which the dispersion and dissipation errors are less than 0.5% for K up to approximately N.

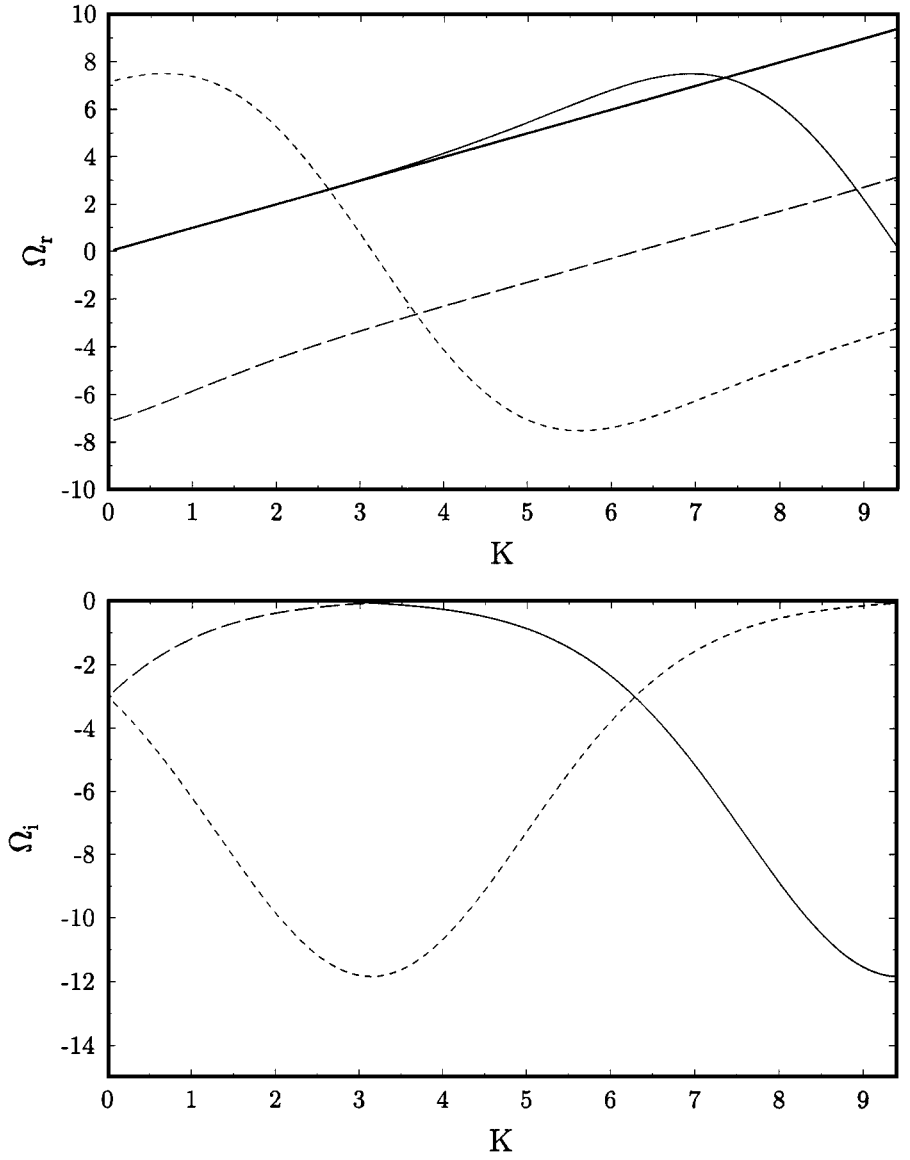

FIG. 1. Numerical dispersion relation (top) and dissipation rate (bottom) for the third-order scheme. The solid line is the physical mode.

To quantify the resolution of the scheme, let us specify the dispersion and dissipation errors to be less than 0.5%, i.e.,

$$|\Omega_r - K| < 0.005 \qquad \text{and} \qquad |\Omega_i| < 0.005. \tag{3.12}$$

The dissipation criterion corresponds to the damping of wave amplitude by less than 10% over a distance of 20 elements. The resolution property of the scheme is quantified in Table I in terms of the maximum resolvable wave number k_c and the number of points per wavelength (computed as $2\pi N/(k_c\delta)$), which is also the number of degrees of freedom per wavelength, satisfying the accuracy limit (3.12) on dispersion and dissipation errors.

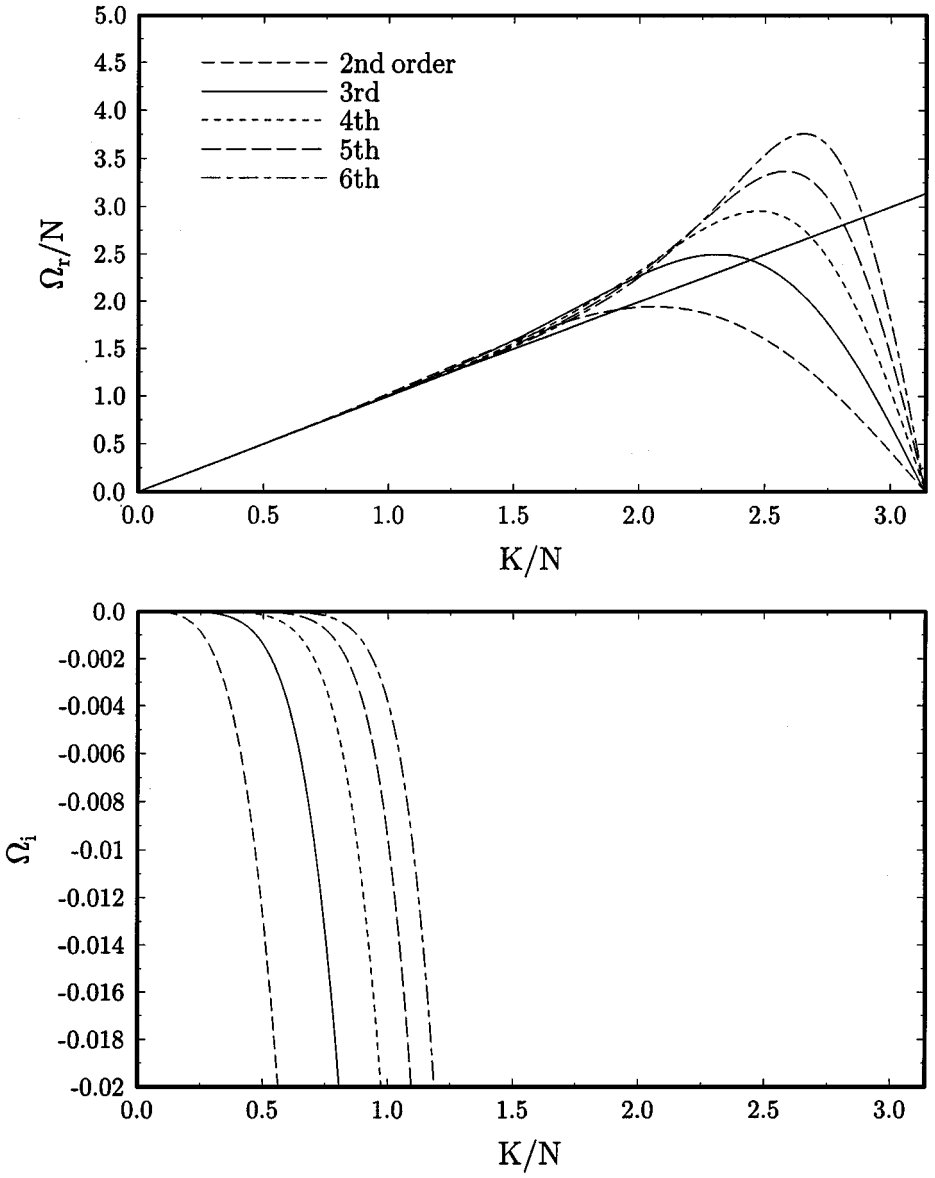

FIG. 2. Numerical dispersion relation (top) and dissipation rate (bottom) of the physical mode for schemes of order 2 to 6.

It is evident from Fig. 2 and Table I that the limit on the dissipation error imposes a relatively more stringent condition on the accuracy of the scheme than does the dispersion error. The resolution property of the various orders of the scheme shown in Table I should serve as a rough guideline, as it is based on the simplest advection equation and arbitrary error bounds (3.12).

Remarks. The numerical dispersion relation naturally depends on the flux formula. The results presented in Figs. 1 and 2 are based on the Roe flux ($\alpha = 1$). The upwinding in the Roe flux introduces a certain amount of damping. In order to illustrate the effect of the flux formula, the dispersion relation using a centered flux ($\alpha = 0$) is plotted in Fig. 3. Shown

TABLE I
Maximum Resolvable Wave Number $k_c\delta$ According to Criteria (3.12)

Order	$k_c\delta$	Points per wavelength
2	0.8	15.7
3	1.8	10.5
4	3.2	7.9
5	4.6	6.8
6	6.15	6.2
8	9.4	5.3
12	16.2	4.6
16	23.35	4.3

Note. Upwind flux ($\alpha = 1$).

therein is the real part of Ω vs K. The imaginary part of Ω is zero, implying no damping. This is true even for parasite waves. However, there is a slight deterioration in the dispersion relation as it starts deviating from the exact one at $K < 3$.

All the numerical results reported here are based on the Legendre polynomials as the basis functions.

3.2. Two-Dimensional Analysis

We now study the numerical dispersion and dissipation errors associated with the discretization of the wave equation

$$\frac{\partial^2\phi}{\partial t^2} - a^2\nabla^2\phi = 0 \tag{3.13}$$

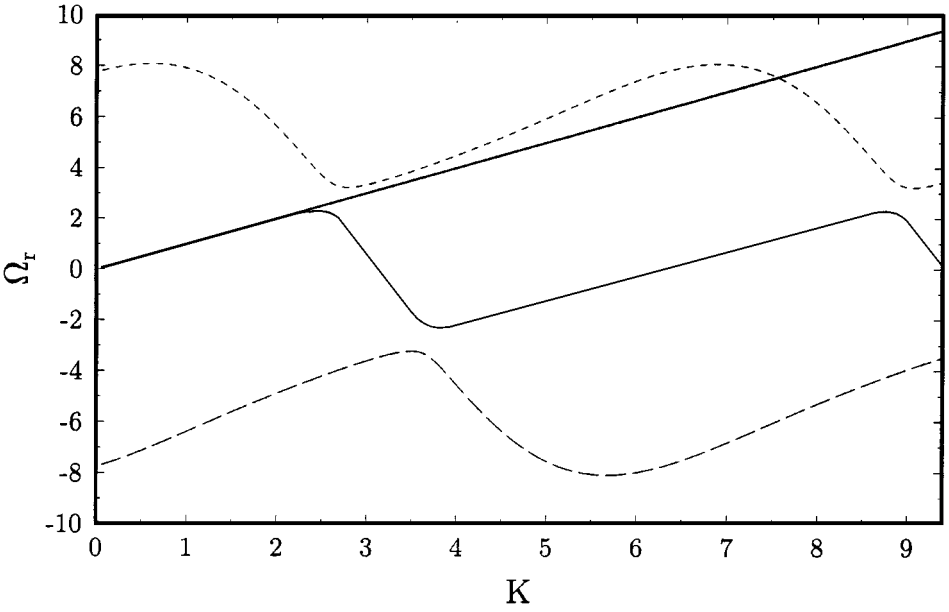

FIG. 3. Numerical dispersion relation for the third-order scheme when a centered flux is used. The imaginary part of Ω is zero for all modes.

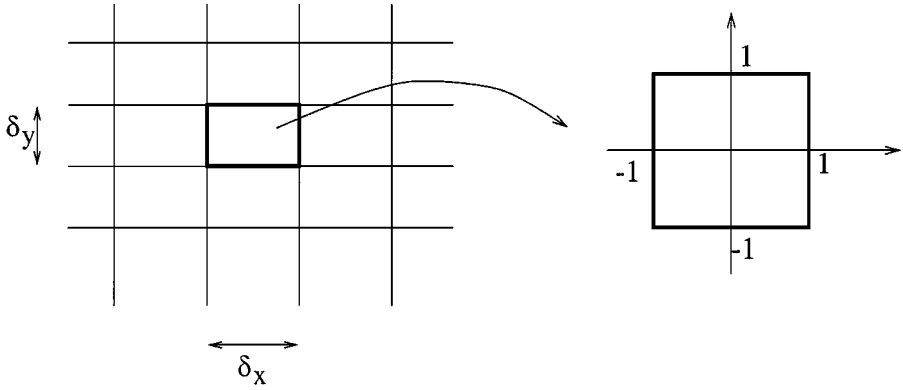

FIG. 4. Rectangular mesh pattern and local coordinate system.

by the discontinuous Galerkin method on quadrilateral and triangular elements. By setting

$$u_1 = \frac{\partial \phi}{\partial t} - a\frac{\partial \phi}{\partial x} \qquad \text{and} \qquad u_2 = -a\frac{\partial \phi}{\partial y},$$

we can write (3.13) in the form of (2.1) where

$$\mathbf{F}(u) = \begin{pmatrix} A_1\mathbf{u} \\ A_2\mathbf{u} \end{pmatrix}, \qquad A_1 = a\begin{pmatrix} 1 & 0 \\ 0 & -1 \end{pmatrix}, \qquad A_2 = a\begin{pmatrix} 0 & 1 \\ 1 & 0 \end{pmatrix}, \tag{3.14}$$

which is expedient for the application of the discontinuous Galerkin method.

3.2.1. *Quadrilateral Elements*

For simplicity, the computational domain is divided into rectangular elements E^{nm} by lines $x = x_n$ and $y = y_m$, i.e., $E^{nm} = [x_n, x_{n+1}] \times [y_m, y_{m+1}]$, as shown in Fig. 4. Then using the Roe flux, (3.2) can be easily rewritten in a matrix form

$$\begin{aligned} &\mathbf{Q}\frac{\partial \mathbf{C}^{nm}}{\partial t} + \frac{2a}{\Delta x_n}\left[\mathbf{N}_0\mathbf{C}^{nm} + \mathbf{N}_{-1}\mathbf{C}^{n-1m} + \mathbf{N}_{+1}\mathbf{C}^{n+1m}\right] \\ &\quad + \frac{2a}{\Delta y_m}\left[\mathbf{M}_0\mathbf{C}^{nm} + \mathbf{M}_{-1}\mathbf{C}^{nm-1} + \mathbf{M}_{+1}\mathbf{C}^{nm+1}\right] = 0, \end{aligned} \tag{3.15}$$

where $\Delta x_n = x_{n+1} - x_n$, $\Delta y_n = y_{n+1} - y_n$, and $\mathbf{C}^{nm}$ denotes the vector containing all the coefficients of expansion in the element E^{nm}. The matrices are given in the Appendix.

As in the one-dimensional analysis, if the mesh is uniform, i.e., $\Delta x_n \equiv \delta_x$, $\Delta y_m \equiv \delta_y$, then we can seek solutions in the form

$$\mathbf{C}^{nm}(t) = \hat{\mathbf{C}}e^{i[k(\cos\theta x_n + \sin\theta y_m) - \omega t]}, \tag{3.16}$$

where $\mathbf{k} = (k\cos\theta, k\sin\theta)$ and $\hat{\mathbf{C}}$ is a complex vector independent of n, m, and t. This represents a plane wave solution with a wave number k and a propagation angle θ. By substituting (3.16) into (3.15), we get

$$\left[-i\omega\mathbf{Q}+\frac{2a}{\delta_x}\left(\mathbf{N}_0+e^{-ik\cos\theta\delta_x}\mathbf{N}_{-1}+e^{ik\cos\theta\delta_x}\mathbf{N}_{+1}\right)\right.$$
$$\left.+\frac{2a}{\delta_y}\left(\mathbf{M}_0+e^{-ik\sin\theta\delta_y}\mathbf{M}_{-1}+e^{ik\sin\theta\delta_y}\mathbf{M}_{+1}\right)\right]\hat{\mathbf{C}}=0. \tag{3.17}$$

That the determinant of the coefficient matrix must be zero for a non-trivial solution of $\hat{\mathbf{C}}$ determines the dispersion relation for the semi-discretization.

Dissipation and dispersion errors. To study the dispersion relation (3.17), we define the following non-dimensional parameters

$$\Omega=\frac{\omega\delta_x}{a},\qquad K=k\delta_x,\qquad \frac{\delta_y}{\delta_x}=\gamma.$$

The exact dispersion relation for (2.1), (3.1), and (3.14) is $\Omega=\pm K$. The numerical dispersion relation is given by

$$\det\left(-i\Omega\mathbf{Q}+2\left(\mathbf{N}_0+e^{-iK\cos\theta}\mathbf{N}_{-1}+e^{iK\cos\theta}\mathbf{N}_{+1}\right)\right.$$
$$\left.+2\gamma\left(\mathbf{M}_0+e^{-iK\sin\theta\gamma}\mathbf{M}_{-1}+e^{iK\sin\theta\gamma}\mathbf{M}_{+1}\right)\right)=0. \tag{3.18}$$

It is clear that the value of Ω will now be a function of wave number K and angle θ. Consequently, the wave propagation will be anisotropic, especially for under-resolved waves.

Using the third-order scheme as an example, the numerical frequency Ω as a function of wave angle θ is shown in Fig. 5 for $K=0.5\pi, 0.8\pi$, and π with $\delta_x=\delta_y$. It is to be noted that as the wave number increases, the dependency on θ increases.

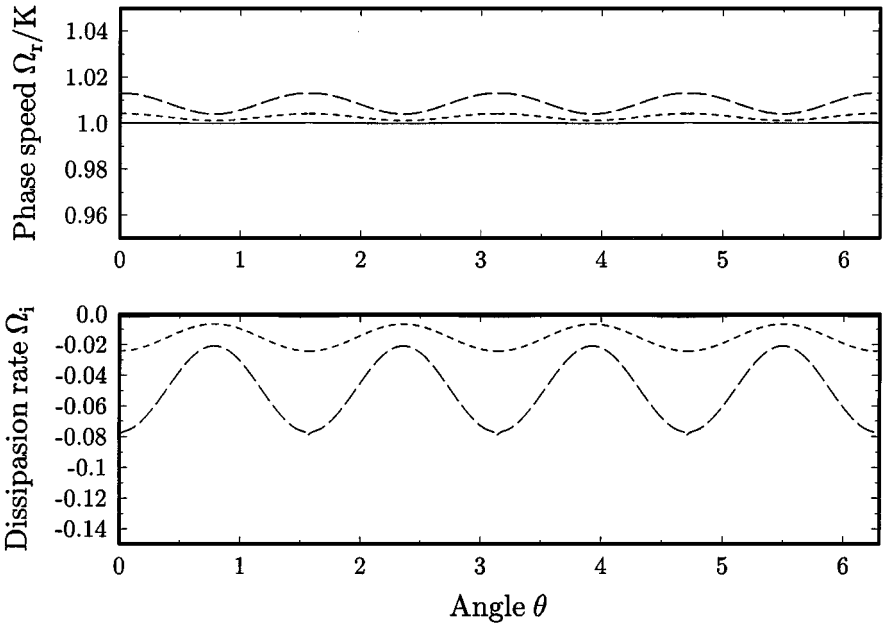

FIG. 5. Numerical phase speed (top) and dissipation rate (bottom) as functions of wave propagation angle θ. Tensor-product basis. $\delta_x=\delta_y$. (—) $K=0.5\pi$; (- - -) $K=0.8\pi$; (– – –) $K=\pi$.

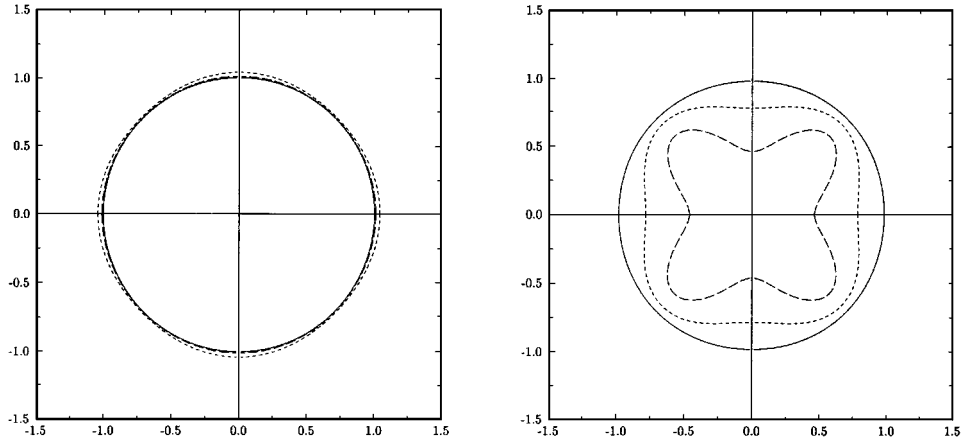

FIG. 6. Polar plot of phase speed Ω_r/K (left) and dissipation $e^{-10|\Omega_i|}$ (right). Tensor-product basis. (—) $K=0.5\pi$; (- - -) $K=0.8\pi$; (– – –) $K=\pi$.

To illustrate the anisotropy more graphically, Fig. 6 shows the numerical *phase speed* and *dissipation rate* as functions of θ in a polar plot. Here, the phase speed is Ω_r/K. The exact dispersion relation is represented by the unit circle. Figure 6 (right) is the polar plot of dissipation $e^{-10|\Omega_i|}$ (i.e., the damping of the wave amplitude over a distance of $10\delta_x$) as a function of θ, and it brings out the anisotropy rather dramatically. Note that the dissipation error is relatively larger than the dispersion error. As such, a simulation of a circular wave in the under-resolved wave space may still appear to be a circle but the wave amplitude will be damped at a rate that varies with the angle θ. It is easy to verify that the dispersion relation given by (3.18) in the direction $\theta=0$ or $\theta=\pi/2$ is the same as the corresponding one-dimensional analysis presented in Section 2. Figure 6 indicates that both the dispersion and dissipation errors are the largest in the direction of $\theta=0$ or $\theta=\pi/2$. This implies that the accuracy limits given in Section 2 still apply here. This is also typical of schemes of other orders.

Remarks. The basis used in the previous example is formed by a tensor product of one-dimensional basis functions. A different basis can be formed by retaining only those polynomials that are necessary for the completeness of the order. We call it the order-complete basis. For a given order N, the number of polynomials in the basis is N^2 for the tensor-product basis and $\frac{1}{2}N(N+1)$ for the order-complete basis.

The phase speed and dissipation rate for the order-complete basis is given in Figs. 7 and 8. Contrary to the tensor-product basis, the largest damping occurs in the diagonal direction of the element. This is not entirely surprising since now fewer basis functions are used.

The anisotropy is significantly reduced as the order of the scheme increases. Figures 9 and 10 show the dissipation rate as a function of θ for $K=\pi$ for schemes of order 3 to 6. Both the tensor-product basis and the order-complete basis show improvement.

3.2.2. *Triangular Elements*

Triangular elements are perhaps more flexible than the quadrilaterals for most mesh generators. For this reason, they are also more popular in applications. Three cases of regular triangular mesh patterns are analysed. They are shown in Fig. 11. In each case, the mesh is generated by repeating a mesh pattern, referred to as the *generating pattern*,

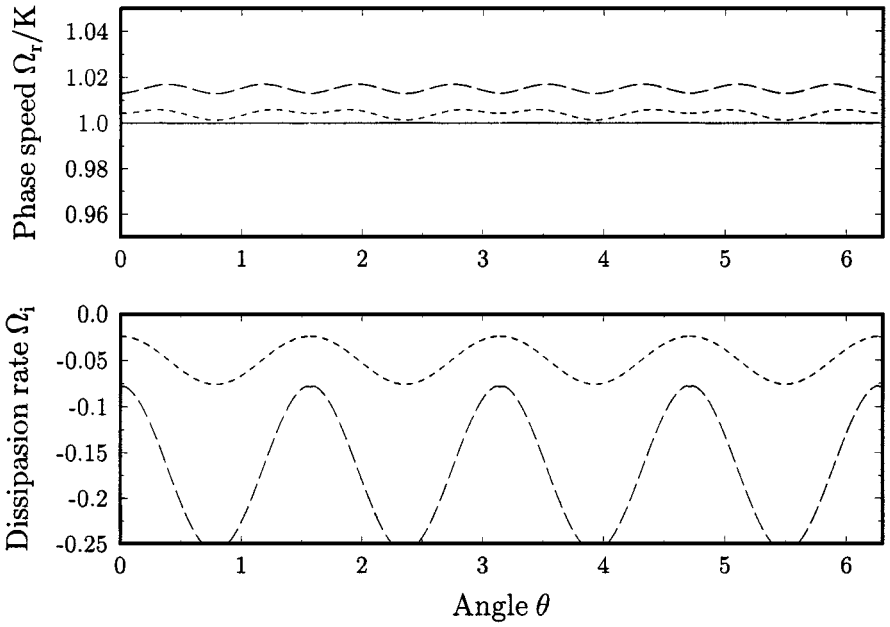

FIG. 7. Numerical phase speed (top) and dissipation rate (bottom) as functions of wave propagation angle θ. Order-complete basis. $\delta_x = \delta_y$. (—) $K = 0.5\pi$; (- - -) $K = 0.8\pi$; (– – –) $K = \pi$.

outlined in dark solid lines. For the meshes in cases 1 and 2, the elements are formed by dividing a rectangular grid along the diagonal lines. In case 1, the resulting elements are similarly oriented while in case 2 the orientations are alternated. Case 3 is included here as it represents a common pattern for many mesh generators.

After computing the expansion coefficients of (3.3), an equation similar to (3.15) can be derived for each case shown in Fig. 11, except that vector $\mathbf{C}^{nm}$ now contains all the coefficients for the elements within the generating pattern. This is a straightforward process and does not warrant any explanation. For the mesh with triangular elements, the order-complete basis is used.

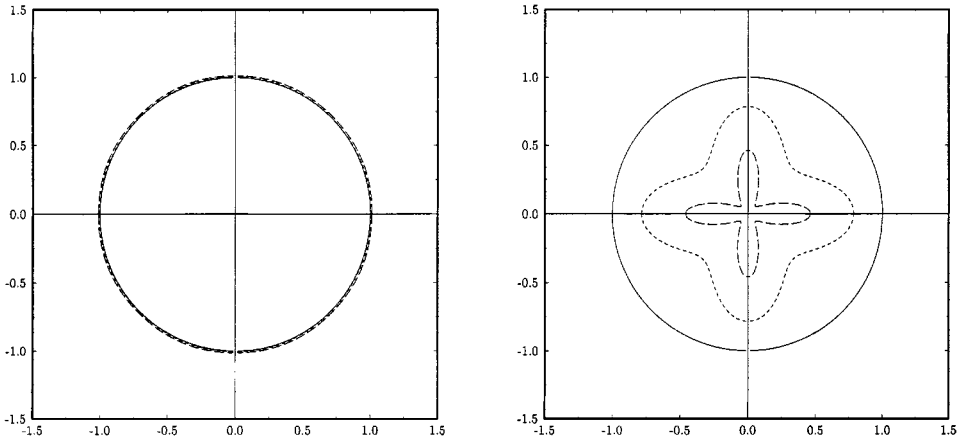

FIG. 8. Polar plot of phase speed Ω_r/K (left) and dissipation $e^{-10|\Omega_i|}$ (right). Order-complete basis. (—) $K = 0.5\pi$; (- - -) $K = 0.8\pi$; (– – –) $K = \pi$.

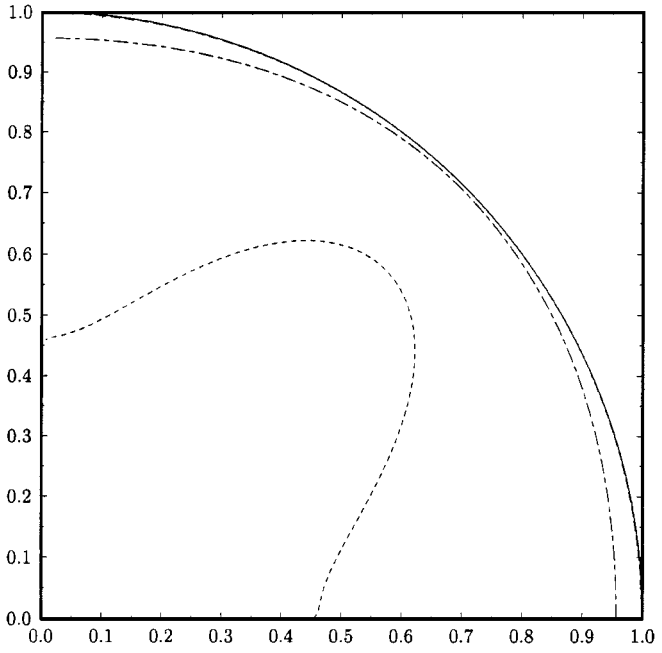

FIG. 9. Dissipation factor ($e^{-10|\Omega_i|}$) as a function of θ for schemes of order 3 to 6. Tensor-product basis. (- - -) Order 3; (– – –) order 4; (– – –) order 5; (—) order 6.

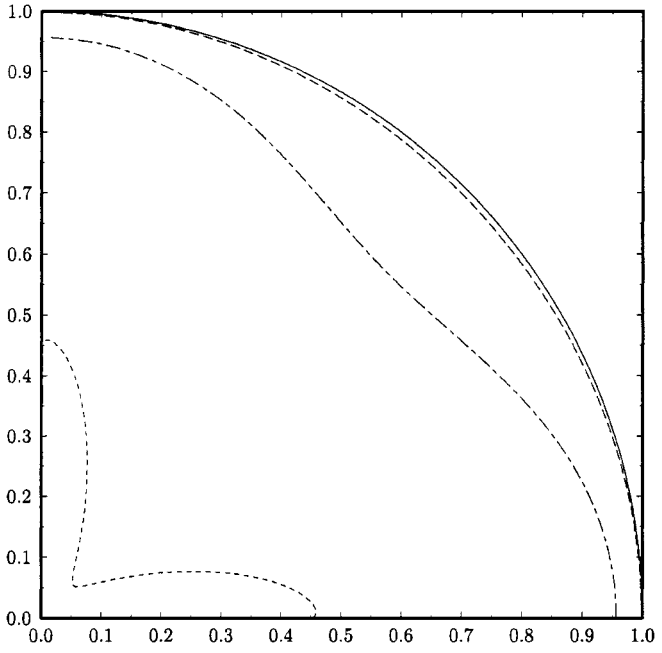

FIG. 10. Dissipation factor ($e^{-10|\Omega_i|}$) as a function of θ for schemes of order 3 to 6. Order-complete basis. (- - -) Order 3; (– – –) order 4; (– – –) order 5; (—) order 6.

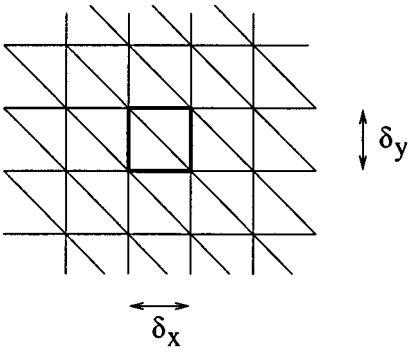

Case 1

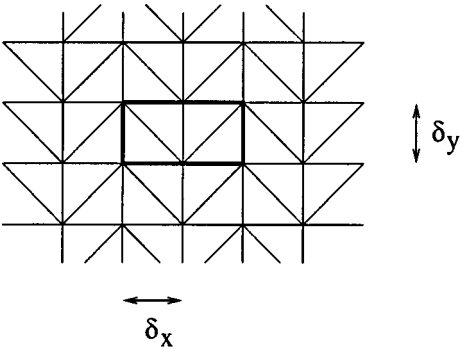

Case 2

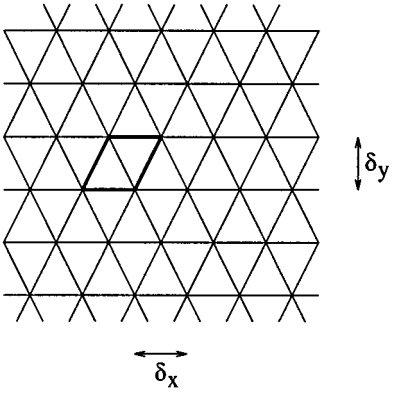

Case 3

FIG. 11. Triangular mesh patterns considered.

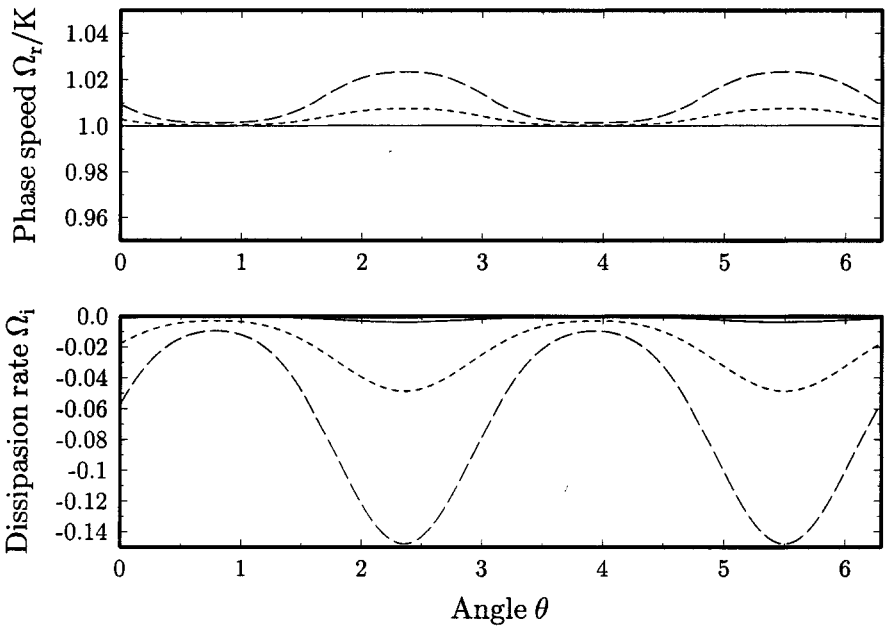

FIG. 12. Numerical phase speed (top) and dissipation rate (bottom) as a function of wave propagation angle θ. Mesh of case 1 in Fig. 11. $\delta_x = \delta_y$. (—) $K = 0.5\pi$; (- - -) $K = 0.8\pi$; (– – –) $K = \pi$.

The third-order scheme is used as an example. For the mesh pattern in case 1, the phase speed Ω as a function of θ is shown in Fig. 12. Figure 13 illustrates the dependency of the phase speed and the dissipation rate on the wave angle θ in a polar plot for $K = 0.5\pi$, 0.8π, and π with $\delta_x = \delta_y$ (the dissipation rate in Fig. 13 (right) represents the damping of the amplitude after the wave has propagated a distance of $10\delta_x$). Figure 13 shows that the wave has a preferred direction of propagation, namely, the direction normal to the diagonal interfaces in Fig. 11 (top).

In the mesh pattern of case 2, the orientation of the elements is not uniform but alternates between two directions. This appears to decrease the anisotropy exhibited in case 1. This

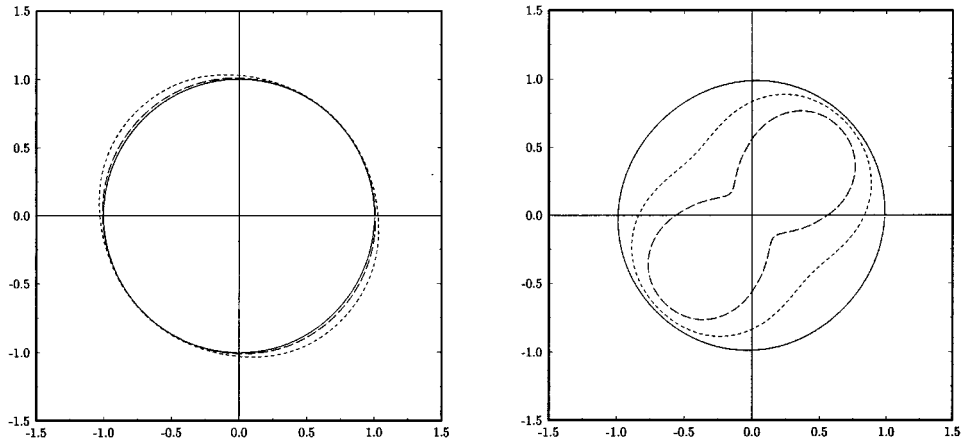

FIG. 13. Polar plot of phase speed Ω_r/K (left) and dissipation $e^{-10|\Omega_i|}$ (right). Mesh of case 1 in Fig. 11. (—) $K = 0.5\pi$; (- - -) $K = 0.8\pi$; (– – –) $K = \pi$.

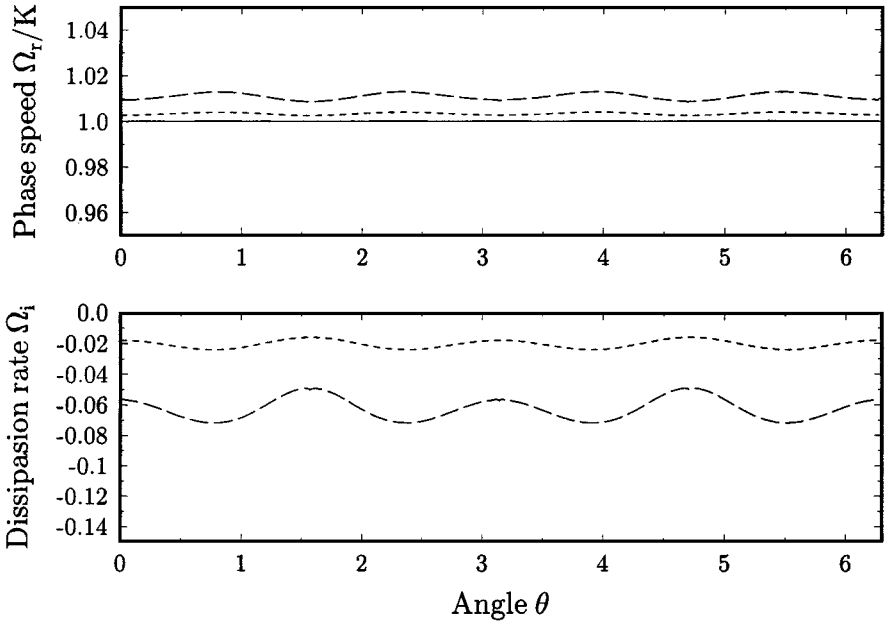

FIG. 14. Numerical phase speed (top) and dissipation rate (bottom) as a function of wave propagation angle θ. Mesh of case 2 in Fig. 11. $\delta_x = \delta_y$. (—) $K = 0.5\pi$; (- - -) $K = 0.8\pi$; (– – –) $K = \pi$.

is evident in Fig. 14 which displays the phase speed Ω as a function of θ for the third-order scheme and in Fig. 15 which shows their respective polar plots.

Case 3 is a common structure in triangular-element grids. The dispersion relation and the dissipation rate displayed in Figs. 16 and 17 indicate a light improvement over the results of case 2.

Numerical dissipation as a function of wave angle θ is shown in Figs. 18 and 19 for cases 2 and 3, respectively. The wave number is $K = \pi$ and the order of the scheme varies from 3 to 6. The higher order schemes tend to have significantly less anisotropy in wave propagation, consistent with the earlier observation.

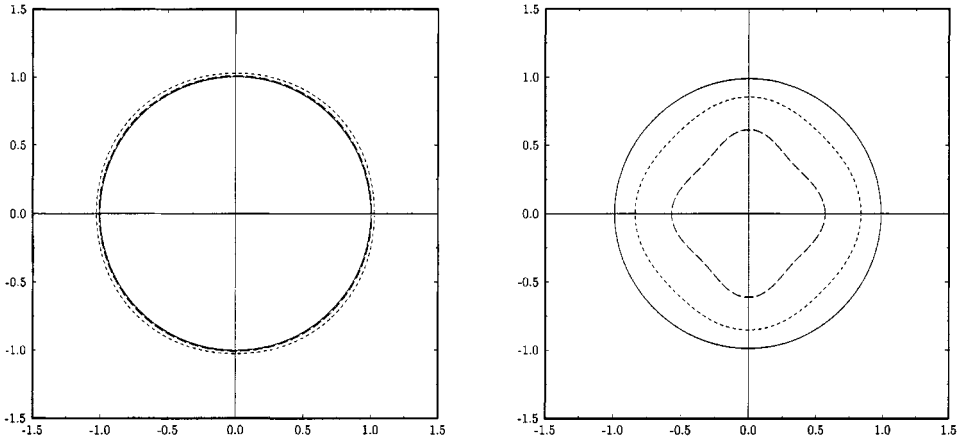

FIG. 15. Polar plot of phase speed Ω_r/K (left) and dissipation $e^{-10|\Omega_i|}$ (right). Mesh of case 2 in Fig. 11. (—) $K = 0.5\pi$; (- - -) $K = 0.8\pi$; (– – –) $K = \pi$.

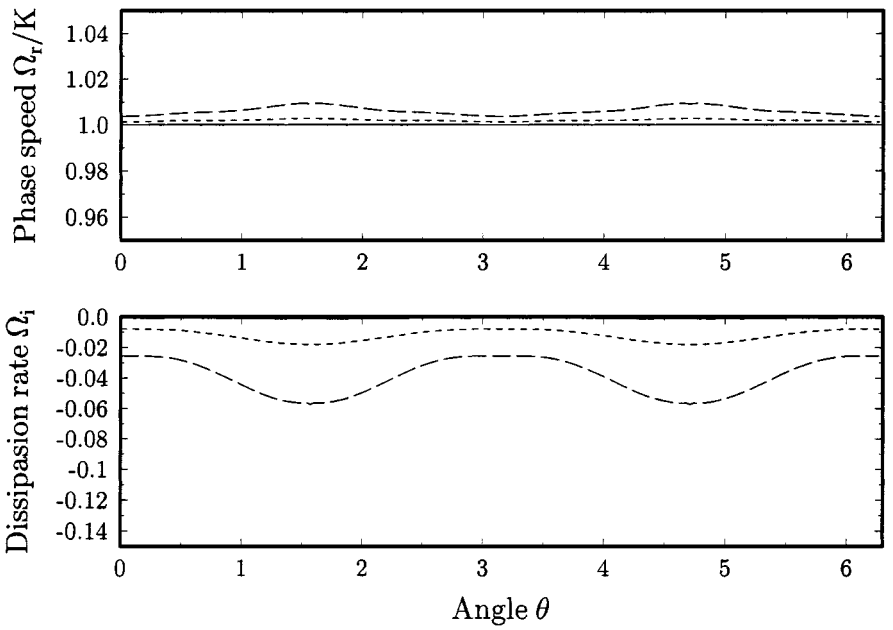

FIG. 16. Numerical phase speed (top) and dissipation rate (bottom) as a function of wave propagation angle θ. Mesh of case 3 in Fig. 11. $\delta_x = \delta_y$. (—) $K = 0.5\pi$; (- - -) $K = 0.8\pi$; (– – –) $K = \pi$.

4. NUMERICAL EXAMPLES

In this section, we present some numerical examples to validate the analysis of the previous sections.

4.1. One-Dimensional Scalar Advection Equation

Equation (3.4) is solved numerically by the Runge–Kutta discontinuous Galerkin method using Legendre polynomials as basis functions on uniform elements with $\delta = 1$. The initial

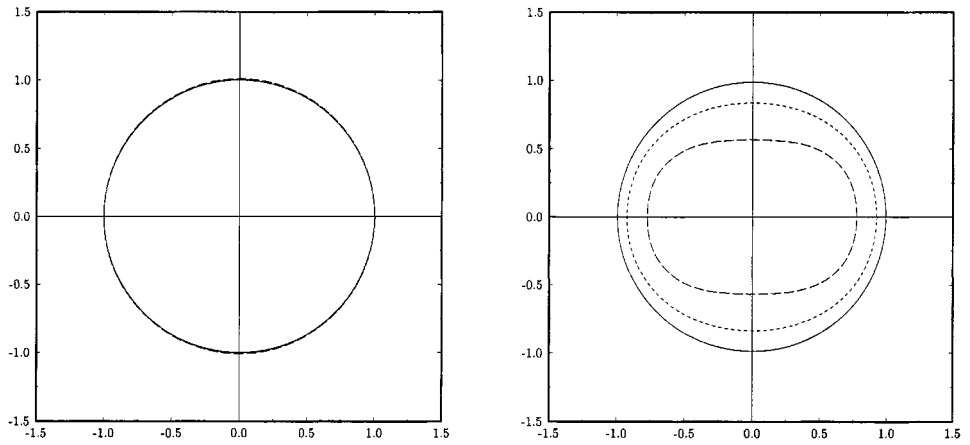

FIG. 17. Polar plot of phase speed Ω_r/K (left) and dissipation $e^{-10|\Omega_i|}$ (right). Mesh of case 3 in Fig. 11. (—) $K = 0.5\pi$; (- - -) $K = 0.8\pi$; (– – –) $K = \pi$.

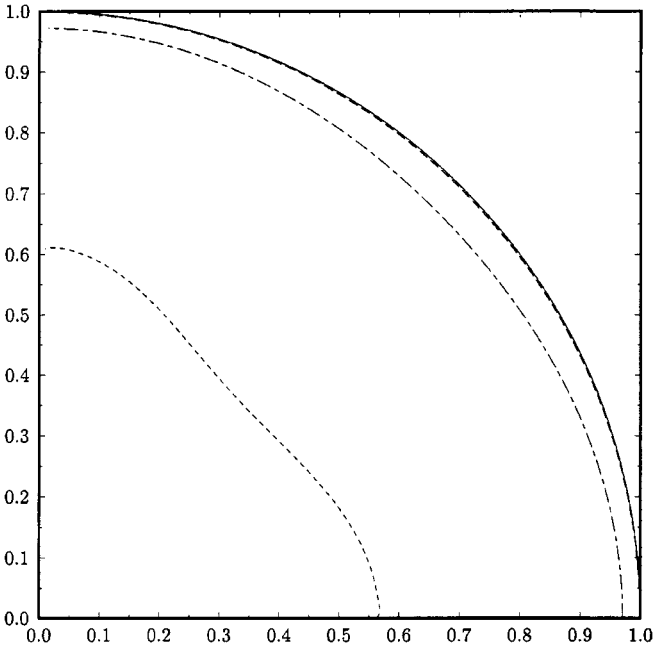

FIG. 18. Dissipation factor ($e^{-10|\Omega_i|}$) as a function of θ for schemes of order 3 to 6. Triangular mesh of case 2 in Fig. 11. (- - -) Order 3; (– - –) order 4; (– – –) order 5; (—) order 6.

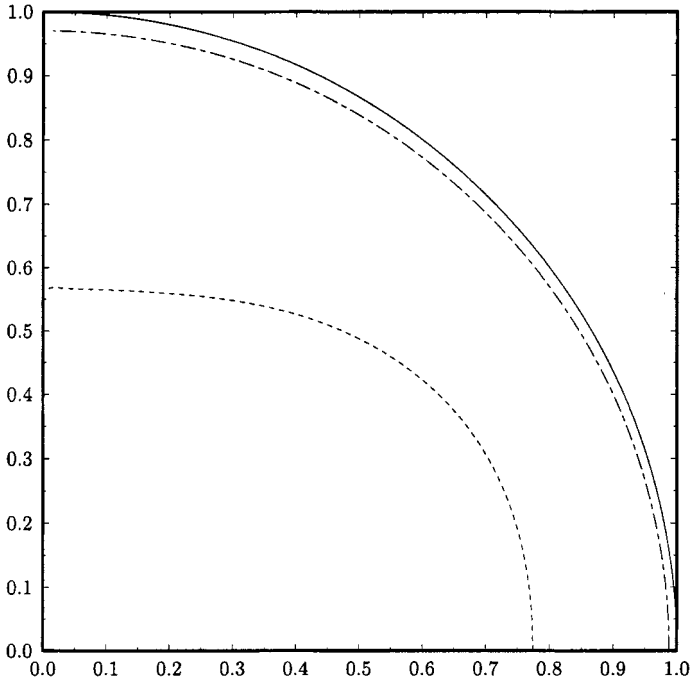

FIG. 19. Dissipation factor ($e^{-10|\Omega_i|}$) as a function of θ for schemes of order 3 to 6. Triangular mesh of case 3 in Fig. 11. (- - -) Order 3; (– - –) order 4; (– – –) order 5; (—) order 6.

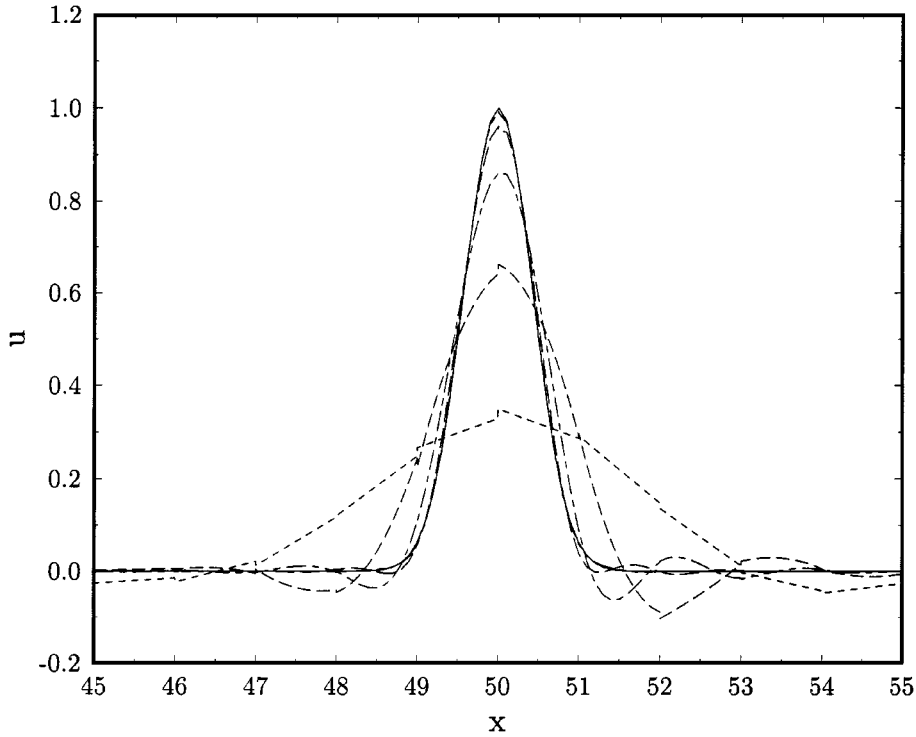

FIG. 20. Numerical solution of Eq. (3.4). Uniform mesh $\delta_x = 1$, $r_0 = 0.5$, $a = 1$. (- - -) Order 2; (– – –) order 3; (– – –) order 4; (— — —) order 5; (– – – –) order 6; (—) exact.

condition is a Gaussian profile

$$u(x, 0) = e^{-\ln 2(x/r_0)^2}, \tag{4.1}$$

where r_0 is assumed to be equal to 0.5. Plotted in Fig. 20 is the solution at time $t = 50$, i.e., after the initial profile has propagated a distance of 50 elements. We observe that the dissipation errors are more significant than the dispersion errors, which is consistent with the predictions in Figs. 1 and 2. Furthermore, the peak of the numerical solution is only slightly ahead of the exact location, confirming that the numerical wave speed is slightly faster than the exact wave speed, as indicated in Figs. 1 and 2.

4.2. Two-Dimensional Acoustic Wave

We solve the non-linear Euler equations (2.1) where

$$\mathbf{u} = \begin{pmatrix} \rho \\ \rho u \\ \rho v \\ E \end{pmatrix}, \qquad \mathbf{F}(\mathbf{u}) = \begin{pmatrix} F_1(\mathbf{u}) \\ F_2(\mathbf{u}) \end{pmatrix}$$

$$F_1(\mathbf{u}) = \begin{pmatrix} \rho u \\ \rho u^2 + p \\ \rho uv \\ u(E + p) \end{pmatrix}, \qquad F_2(\mathbf{u}) = \begin{pmatrix} \rho v \\ \rho uv \\ \rho v^2 + p \\ v(E + p) \end{pmatrix}$$

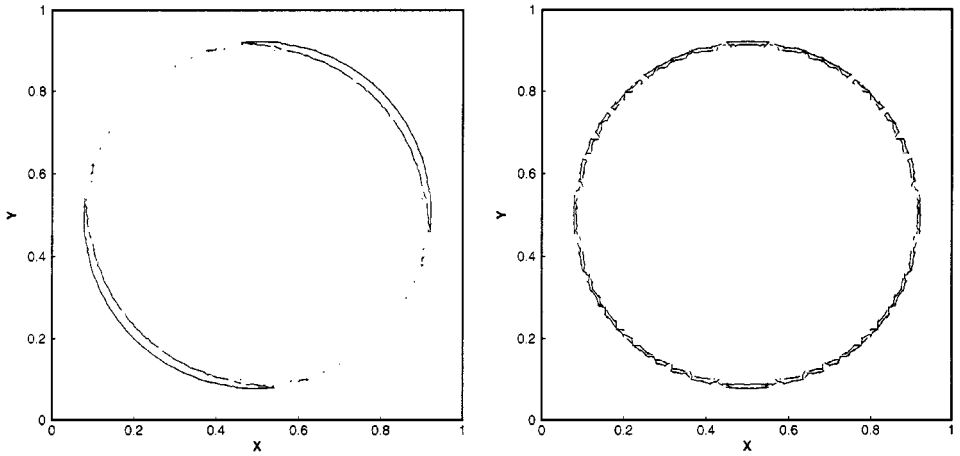

FIG. 21. Pressure contours (level 1.00005) with grid 1 (left) and grid 2 (right). Order 2 scheme.

on a square domain $[0, 1] \times [0, 1]$ with the initial condition

$$\rho(x, y, 0) = 1, \qquad u(x, y, 0) = 0, \qquad v(x, y, 0) = 0$$

and

$$p(x, y, 0) = 1 + 0.001e^{-\ln(2)\frac{(x-0.5)^2+(y-0.5)^2}{r_0^2}}, \qquad r_0 = 0.02,$$

which represents a small acoustic source at the center of the domain.

The computations are carried out on three different grids. Grids 1 and 2 are (50×50) structured grids with the mesh patterns shown in Fig. 11 as cases 1 and 2, respectively. Grid 3 is unstructured as shown in Fig. 24. The numerical scheme employs first-order polynomials (second-order scheme) to fourth-order polynomials (fifth order scheme), and a third-order Runge–Kutta time stepping with a CFL (Courant–Friedrich–Lewy) number equal to 0.25. The time step was chosen small enough such that the errors are dominated by the spatial discretization errors.

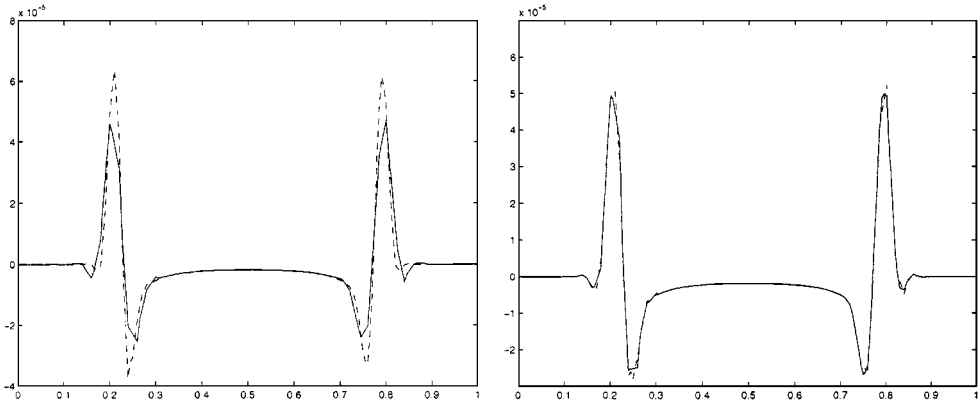

FIG. 22. Pressure profiles $p - 1$ along $x = y$ (- - -) and $x = -y$ (—) with grid 1 (left) and grid 2 (right). Order 2 scheme.

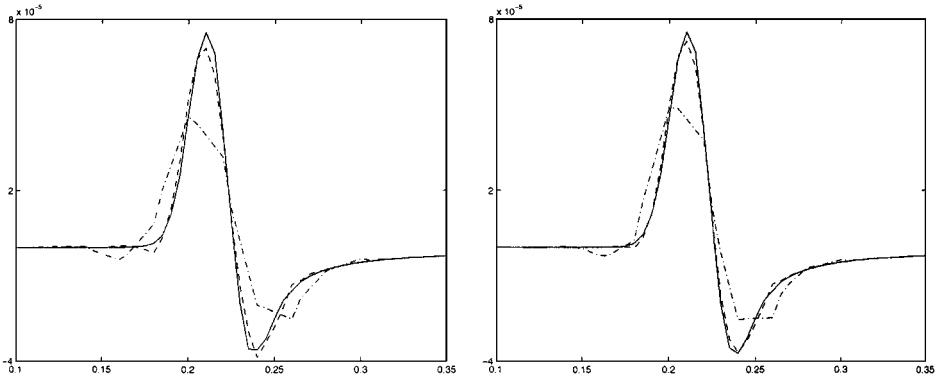

FIG. 23. Pressure profiles $p-1$ along $x=-y$ on grid 1 (left) and grid 2 (right). (– · –) Order 2; (- - -) order 3; (—) order 4. Only the left peak is displayed.

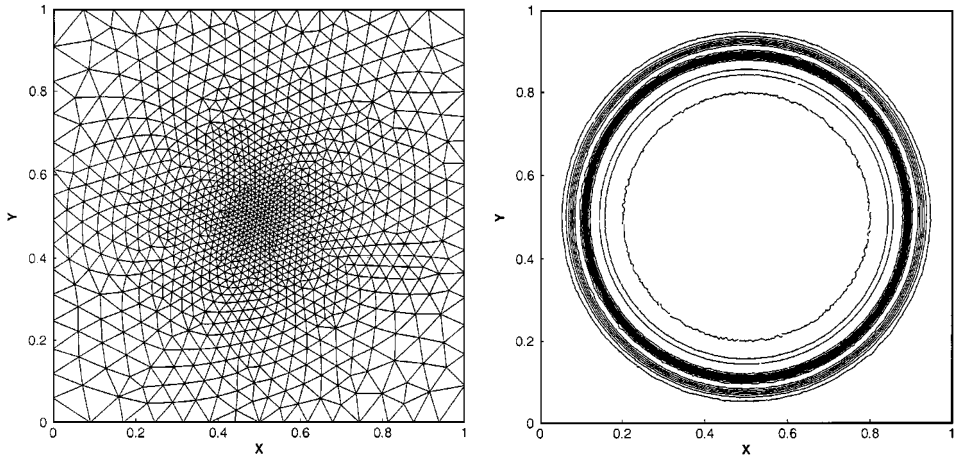

FIG. 24. Unstructured triangular grid containing 1201 points (left) and pressure contours (level 0.999973 to 1.00007) for an order 5 scheme (right).

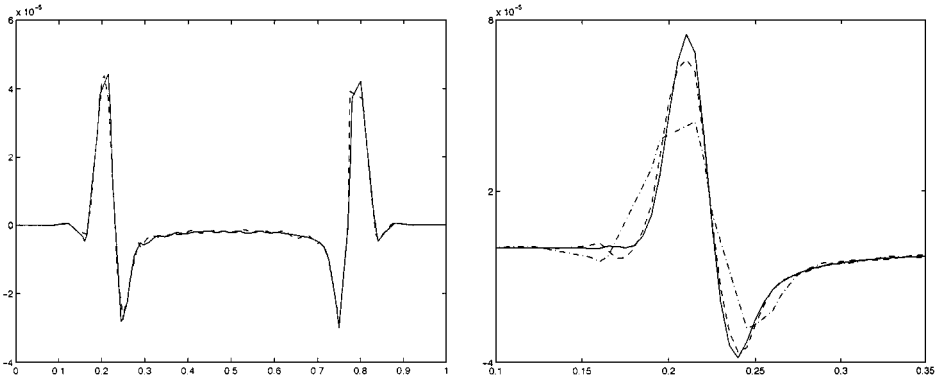

FIG. 25. (Left) Pressure profiles $p-1$ along $x=y$ (- - -) and along $x=-y$ (—) for an order 2 scheme. (Right) Pressure profiles $p-1$ along $x=-y$ for (– · –) order 2, (- - -) order 3, and (—) order 4 schemes. Only the left peak is displayed.

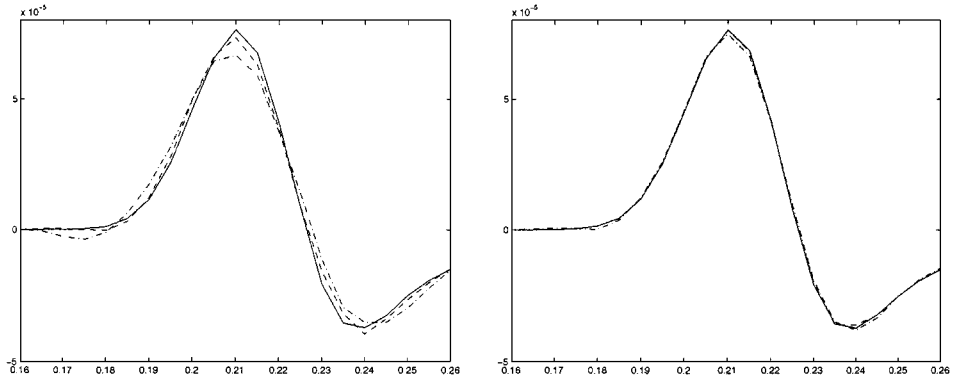

FIG. 26. Pressure profiles $p-1$ along $x=y$ (only the left peak is displayed) for an order 3 (left) and an order 4 (right) scheme. (– · –) Unstructured mesh, (- - -) grid 2, and (—) grid 1.

Figure 21 presents the pressure contours obtained with the second-order scheme on grids 1 and 2 after the wave has propagated a distance of 20 r_0. The pressure profile along the diagonal lines $x=y$ and $x=-y$ are displayed in Fig. 22. These results are found to agree with the analytical predictions: errors in the form of anisotropy in wave propagation (i.e., the amplitude is a function of wave angle) are introduced by grid 1, whereas such errors on grid 2 are relatively small. Figure 23 shows the pressure profile along $x=-y$ on grids 1 and 2 for schemes of order 2 to 4. The dissipation error is found to dominate; it decrease significantly as also the anisotropy with the increase in the order of the scheme.

Numerical results obtained on the unstructured grid are presented in Figs. 24 and 25. These results are similar to those obtained on the structured grids. The dissipation errors are more pronounced than those on the first two grids. On the other hand, anisotropy is less apparent even for the second-order scheme. Figure 26 compares the results obtained on the three different grids with a third-order and a fourth-order scheme. It appears that the influence of the mesh structure on the dissipation error decreases as the order of the scheme increases.

5. CONCLUSIONS

The present study of a discontinuous Galerkin method shows that the dispersion relation and the dissipation rate depend on the flux formula. Specifically, in the case of a scalar advection equation, it is shown that the dissipation error is dominant relative to the dispersion error if an upwind flux is used. The choice of the order of the method is then determined by the accuracy limit imposed on the dissipation error; the dispersion relation is almost exactly satisfied for non-dimensional wave numbers up to a value equal to the order of the method. For the centered flux, the dissipation rate is exactly zero, but the range of wave numbers for which the discrete dispersion relation accurately approximates the exact one is relatively small. This suggests the possibility of an optimal flux formula which will yield minimal dispersion and dissipation errors over a range of wave numbers. It is the subject of our ongoing study.

The orientation of elements in a mesh introduces anisotropy in the phase speed as well as the damping rate. The anisotropy in the dissipation rate is more pronounced than that in the dispersion relation. It was shown earlier that the mesh with alternating-orientation

elements has less anisotropic error than that with uniform orientation. The unstructured mesh engenders less anisotropy compared to the structured mesh with triangular or quadrilateral elements with uniform orientation or alternating orientations.

The discontinuous Galerkin methods have the potential to become a practical alternative to the current finite difference methods for acoustic and electromagnetic wave propagation problems. These methods easily accommodate increasing order of accuracy as desired while preserving compactness. They also easily handle unstructured grids and boundary conditions. The existing finite-volume codes can be easily modified to adopt these methods. Research is under way for implementing these algorithms for the study of supersonic jet acoustics and certain canonical problems in electromagnetics.

APPENDIX

In this appendix, we give the matrices that appear in Eqs. (3.6) and (3.15) of Section 3.

For the one-dimensional equation (3.4), the flux $F = au$. Using the Roe flux formula ($\alpha = 1$), it follows that $A_\alpha^+ = a$, $A_\alpha^- = 0$.

Let the basis functions be $\{v_l(\bar{x}) | l = 0, 1, \ldots, N-1\}$, where $\bar{x}$ is the local coordinate, $\bar{x} \in [-1, 1]$. The matrices in Eq. (3.6) are formed as

$$\{\mathbf{Q}\}_{ij} = \int_{-1}^{1} v_i v_j \, d\bar{x},$$

$$\{\mathbf{N}_0\}_{ij} = v_i(1) v_j(1) - \int_{-1}^{1} \frac{dv_i}{d\bar{x}} v_j \, d\bar{x},$$

and

$$\{\mathbf{N}_{-1}\}_{ij} = -v_i(-1) v_j(1),$$

where $\{\cdot\}_{ij}$ denotes the entries of the matrix for $i, j = 0, 1, 2, \ldots, N-1$.

For the two-dimensional system (3.14), let

$$\mathbf{A} = \begin{pmatrix} 1 & 0 \\ 0 & -1 \end{pmatrix}, \qquad \mathbf{B} = \begin{pmatrix} 0 & 1 \\ 1 & 0 \end{pmatrix}.$$

They are split according to the eigenvalues as follows:

$$\mathbf{A}^+ = \begin{pmatrix} 1 & 0 \\ 0 & 0 \end{pmatrix}, \quad \mathbf{A}^- = \begin{pmatrix} 0 & 0 \\ 0 & -1 \end{pmatrix}, \quad \mathbf{B}^+ = \begin{pmatrix} \frac{1}{2} & \frac{1}{2} \\ \frac{1}{2} & \frac{1}{2} \end{pmatrix}, \quad \mathbf{B}^- = \begin{pmatrix} -\frac{1}{2} & \frac{1}{2} \\ \frac{1}{2} & -\frac{1}{2} \end{pmatrix}.$$

Let the basis functions be $\{v_l(\bar{x}, \bar{y}) | l = 0, 1, \ldots, L-1\}$. The entries of the matrices in Eq. (3.15) are

$$\{\mathbf{Q}\}_{ij} = \delta_{\alpha\beta} \int_{-1}^{1} \int_{-1}^{1} v_l' v_l \, d\bar{x} d\bar{y} \qquad (\delta_{\alpha\beta} = 1 \text{ if } \alpha = \beta \text{ and } 0 \text{ if } \alpha \neq \beta),$$

$$\{\mathbf{N}_0\}_{ij} = \{\mathbf{A}^+\}_{\alpha\beta} \int_{-1}^{1} v_{l'}(1, \bar{y}) v_l(1, \bar{y}) \, d\bar{y} - \{\mathbf{A}^-\}_{\alpha\beta} \int_{-1}^{1} v_{l'}(-1, \bar{y}) v_l(-1, \bar{y}) \, d\bar{y}$$

$$- \{\mathbf{A}\}_{\alpha\beta} \int_{-1}^{1} \int_{-1}^{1} \frac{\partial v_{l'}}{\partial \bar{x}} v_l \, d\bar{x} \, d\bar{y},$$

$$\{\mathbf{N}_{+1}\}_{ij} = \{\mathbf{A}^-\}_{\alpha\beta} \int_{-1}^{1} v_{l'}(1, \bar{y}) v_l(-1, \bar{y})\, d\bar{y},$$

$$\{\mathbf{N}_{-1}\}_{ij} = -\{\mathbf{A}^+\}_{\alpha\beta} \int_{-1}^{1} v_{l'}(-1, \bar{y}) v_l(1, \bar{y})\, d\bar{y},$$

$$\{\mathbf{M}_0\}_{ij} = \{\mathbf{B}^+\}_{\alpha\beta} \int_{-1}^{1} v_{l'}(\bar{x}, 1) v_l(\bar{x}, 1)\, d\bar{x} - \{\mathbf{B}^-\}_{\alpha\beta} \int_{-1}^{1} v_{l'}(\bar{x}, -1) v_l(\bar{x}, -1)\, d\bar{x}$$
$$- \{\mathbf{B}\}_{\alpha\beta} \int_{-1}^{1} \int_{-1}^{1} \frac{\partial v_{l'}}{\partial \bar{x}} v_l\, d\bar{x}\, d\bar{y},$$

$$\{\mathbf{M}_{+1}\}_{ij} = \{\mathbf{B}^-\}_{\alpha\beta} \int_{-1}^{1} v_{l'}(\bar{x}, 1) v_l(\bar{x}, -1)\, d\bar{x},$$

$$\{\mathbf{M}_{-1}\}_{ij} = -\{\mathbf{B}^+\}_{\alpha\beta} \int_{-1}^{1} v_{l'}(\bar{x}, -1) v_l(\bar{x}, 1)\, d\bar{x},$$

where $i = 2l' + \alpha$, $j = 2l + \beta$ for $\alpha, \beta = 0, 1$ and $l', l = 0, 1, \ldots, N - 1$.

ACKNOWLEDGMENTS

The authors thank Jack Seiner of NASA Langley Research Center and Arje Nachman of AFOSR for the encouragement to carry out this research. F.Q.H. and P.R. are pleased to acknowledge the support of the Program in Computational Science and Engineering at Florida State University.

REFERENCES

1. N. N. Abboud and P. M. Pinsky, Finite-element dispersion analysis for the 3-dimensional 2nd-order scalar wave-equation, *Int. J. Numer. Methods Eng.* **35**, 1183 (1992).
2. H. L. Atkins and C.-W. Shu, *Quadrature-Free Implementation of Discontinuous Galerkin Method for Hyperbolic Equations*, ICASE Report 96-51 (1996).
3. F. Bassi and S. Rebay, A high-order accurate discontinuous finite element method for the numerical solution of the compressible Navier–Stokes equations, *J. Comput. Phys.* **131**, 267 (1997).
4. K. S. Bey and J. T. Oden, $h - p$-version discontinuous Galerkin methods for hyperbolic conservation laws, *Comput. Methods Appl. Mech. Eng.* **133**, 259 (1996).
5. R. Biswas, K. D. Devine, and J. Flaherty, Parallel, adaptive finite element methods for conservation laws, *Appl. Numer. Math.* **14**, 255 (1994).
6. A. Bossavit, A rationale for "edge elements" in 3-D fields computations, *IEEE Trans. Mag.* **24**, 74 (1988).
7. G. Chavent and B. Cockburn, The local projection P^0P^1-discontinuous-Galerkin finite element method for scalar conservation laws, *RAIRO, Model. Math. Anal. Numer.* **23**, 565 (1989).
8. D. J. Chaffin and A. J. Baker, On Taylor weak statement finite-element methods for computational fluid dynamics, *Int. J. Numer. Methods Fluids* **21**, 273 (1995).
9. B. Cockburn and C.-W. Shu, The Runge–Kutta local projection P^1-discontinuous-Galerkin method for scalar conservation laws, *RAIRO, Model. Math. Anal. Numer.* **25**, 337 (1991).
10. B. Cockburn and C.-W. Shu, TVB Runge–Kutta local projection discontinuous Galerkin finite element method for conservation laws. II. General framework, *Math. Comput.* **52**, 411 (1989).
11. B. Cockburn, S. Y. Lin, and C.-W. Shu, TVB Runge–Kutta local projection discontinuous Galerkin finite element method for conservation laws. III. One dimensional systems, *J. Comput. Phys.* **84**, 90 (1989).
12. B. Cockburn, S. Hou, and C.-W. Shu, TVB Runge–Kutta local projection discontinuous Galerkin finite element method for conservation laws. IV. The multidimensional case, *Math. Comput.* **54**, 545 (1990).

13. B. Cockburn and C.-W. Shu, The Runge–Kutta discontinuous Galerkin finite-element method for conservation laws. V. Multidimensional systems, *J. Comput. Phys.* **141**, 199 (1998).
14. B. Cockburn and C.-W. Shu, *The Local Discontinuous Galerkin Method for Time-Dependent Convection-Diffusion Systems*, ICASE Report 97-32 (1997).
15. S. K. Godunov, Finite difference method for numerical computation of discontinuous solutions of fluid dynamics, *Math. Sbornik.* **47**, 251 (1959). [In Russian]
16. F. Q. Hu, M. Y. Hussaini, and J. L. Manthey, Application of low dissipation and dispersion Runge–Kutta schemes to benchmark problems in computational aeroacoustics, in *Proceedings, ICASE/LaRC Workshop on Benchmark Problems in Computational Aeroacoustics, Hampton, Virginia, October 1994*, edited by J. C. Hardin, J. R. Ristorcelli, and C. K. W. Tam, NASA Conference Publication 3300, 1995.
17. F. Q. Hu, M. Y. Hussaini, and J. L. Manthey, Low-dissipation and low-dispersion Runge–Kutta schemes for computational acoustics, *J. Comput. Phys.* **124**, 177 (1996).
18. A. Khelifa and Y. Ouellet, Analysis of time-varying errors in quadratic finite-element approximation of hyperbolic problems, *Int. J. Numer. Methods Eng.* **38**, 3933 (1995).
19. C. Johnson and J. Pitkäranta, An analysis of the discontinuous Galerkin method for a scalar hyperbolic equation, *Math. Comput.* **46**, 1 (1986).
20. S. K. Lele, Compact finite difference schemes with spectral-like resolution, *J. Comput. Phys.* **103**, 16 (1992).
21. P. Lesaint and P. A. Raviart, On a finite element method for solving the neutron transport equation, in *Mathematical Aspects of Finite Elements in Partial Differential Equations* (Academic Press, San Diego, 1974), p. 89.
22. Y. Liu, Fourier analysis of numerical algorithms for the Maxwell equations, *J. Comput. Phys.* **124**, 396 (1996).
23. R. B. Lowrie, *Compact Higher-Order Numerical Methods for Hyperbolic Conservation Laws*, Ph.D. dissertation, The University of Michigan (1996).
24. R. B. Lowrie, P. L. Roe, and B. Van Leer, *A Space-Time Discontinuous Galerkin Method for the Time-Accurate Numerical Solution of Hyperbolic Conservation Laws*, AIAA Paper 95-1658 (1995).
25. C. Makridakis and P. Monk, Time-discrete finite element schemes for Maxwell's equations, *RAIRO, Model. Math. Anal. Numer.* **29**, 171 (1995).
26. G. Mur, The finite-element modeling of three-dimensional time-domain electromagnetic fields in strongly inhomogeneous media, *IEEE Trans. Mag.* **28**, 1130 (1992).
27. T. Peterson, A note on the convergence of the discontinuous Galerkin method for a scalar hyperbolic equation, *SIAM J. Numer. Anal.* **28**, 133 (1991).
28. W. H. Reed and T. R. Hill, *Triangular Mesh Methods for the Neutron Transport Equation*, Los Alamos Scientific Laboratory Report LA-UR-73-479 (1973).
29. G. R. Richter, An optimal-order error estimate for the discontinuous Galerkin method, *Math. Comput.* **50**, 75 (1988).
30. F. Shakib and T. J. R. Hughes, A new finite element formulation for computational fluid dynamics. IX. Fourier analysis of space-time Galerkin/least-squares algorithms. *Comput. Methods Appl. Mech. Eng.* **87**, 35 (1991).
31. J. S. Shang, *High-Order Compact-Difference Schemes for Time-Dependent Maxwell Equations*, AIAA Paper 98-2471 (1998).
32. J. Steger and R. F. Warming, Flux vector splitting of the inviscid gas-dynamic equations with applications to the finite difference methods, *J. Comput. Phys.* **40**, 263 (1981).
33. C. K. W. Tam and J. W. Webb, Dispersion-relation-preserving finite difference schemes for computational acoustics, *J. Comput. Phys.* **107**, 262 (1993).
34. L. L. Thompson and P. M. Pinsky, Complex wave-number Fourier-analysis of the p-version finite element method, *Comput. Mech.* **13**, 255 (1994).
35. T. C. Waburton, I. Lomtev, R. M. Kirby, and G. Karniadakis, *A Discontinuous Galerkin Method for the Compressible Navier–Stokes Equations on hybrid grids*, Technical Report, Center for Fluid Mechanics, Brown University, 97-14 (1997).
36. J. Y. Wu and R. Lee, The advantages of triangular and tetrahedral edge elements for electromagnectic modeling with the finite-element method, *IEEE Trans. Antennas and Propagation* **45**, 1431 (1997).